TOMOGRAPHY® RESEARCH ARTICLE

R2* Relaxation Affects Pharmacokinetic Analysis of Dynamic Contrast-Enhanced MRI in Cancer and Underestimates Treatment Response at 7 T

Jana Kim[1,2], Siver A. Moestue[1,3,4], Tone F. Bathen[1,2], and Eugene Kim[1,5]

[1]Department of Circulation and Medical Imaging, Faculty of Medicine, NTNU - Norwegian University of Science and Technology, Trondheim, Norway; [2]St. Olavs Hospital, Trondheim, Norway; [3]Department of Laboratory Medicine, Women's and Children's Health, NTNU - Norwegian University of Science and Technology, Trondheim, Norway; [4]Department of Pharmacy, Faculty of Health Sciences, Nord University, Namsos, Norway; and [5]Department of Neuroimaging, Institute of Psychiatry, Psychology & Neuroscience, King's College London, London, England

Corresponding Author:
Eugene Kim, PhD
Department of Neuroimaging, Institute of Psychiatry, Psychology and Neuroscience, King's College, London, James Black Centre, 125 Coldharbour Lane, London, SE5 9NU, UK;
E-mail: eugene.kim@kcl.ac.uk

Key Words: DCE-MRI, r2* correction, transverse relaxation, multi-echo, treatment monitoring
Abbreviations: Dynamic contrast-enhanced magnetic resonance imaging (DCE-MRI), magnetic resonance (MR), dynamic susceptibility contrast (DSC), regions of interest (ROI), T2-weighted (T2w), variable repetition times (VTR), echo time (TE), pharmacokinetic (PK)

ABSTRACT

Effective transverse relaxivity of gadolinium-based contrast agents is often neglected in dynamic contrast-enhanced magnetic resonance imaging (DCE-MRI). Here, we assess time and tissue dependence of R2* enhancement and its impact on pharmacokinetic parameter quantification and treatment monitoring. Multiecho DCE-MRI was performed at 7 T on mice bearing subcutaneous TOV-21G human ovarian cancer xenografts (n = 8) and on the transgenic adenocarcinoma of the mouse prostate (TRAMP) model (n = 7). Subsequently, the TOV-21G tumor-bearing mice were treated with bevacizumab and rescanned 2 days later. Pharmacokinetic analysis (extended Tofts model) was performed using either the first echo signal only (standard single-echo DCE-MRI) or the estimated signal at TE = 0 derived from exponential fitting of R2* relaxation (R2*-corrected). Neglecting R2* enhancement causes underestimation of Gd-DOTA concentration (peak enhancement underestimated by 9.4%–16% in TOV-21G tumors and 13%–20% in TRAMP prostates). Median K^{trans} and v_e were underestimated in every mouse (TOV-21G K^{trans}: 11%–19%, TOV-21G v_e: 5.3%–8.9%; TRAMP K^{trans}: 8.6%–19%, TRAMP v_e: 12%–21%). Bevacizumab treatment reduced K^{trans} in all TOV-21G tumors after 48 hours. Treatment effect was significantly greater in all tumors after R2* correction (median change of $-0.050\ min^{-1}$ in R2*-corrected K^{trans} vs. $-0.037\ min^{-1}$ in uncorrected K^{trans}). R2* enhancement in DCE-MRI is both time- and tissue-dependent and may not be negligible at 7 T in tissue with high K^{trans}. This has consequences for the use of K^{trans} and other DCE-MRI parameters as biomarkers, because treatment effect size can be underestimated when R2* enhancement is neglected.

INTRODUCTION

Dynamic contrast-enhanced (DCE) magnetic resonance imaging (MRI) is used to characterize tissue vascularization by tracking the distribution of an intravenously injected gadolinium (Gd)-based contrast agent in tissue over the course of several minutes. These paramagnetic contrast agents change the relaxation times of tissue water protons, thereby influencing the signal intensity in the images. As the net impact on signal intensity depends on the concentration of a contrast agent in a given volume, the serial magnetic resonance (MR) images provide qualitative or quantitative information on contrast agent pharmacokinetics. DCE-MRI is often employed in cancer diagnosis and treatment monitoring, as neoangiogenesis in tumors creates tortuous and leaky blood vessels that result in irregular contrast agent pharmacokinetics (1). Moreover, it is frequently used to characterize blood–brain barrier disruption (2, 3), myocardial perfusion (4), or muscular perfusion (5).

Substantial efforts have been made in recent years to establish recommendations for DCE-MRI at the commonly used field strengths of 1.5 T and 3 T (6-8). Several pharmacokinetic models have been developed to extract quantitative information on vascular structure and function (9). But the accelerating adoption of high field scanners, to the point where MRI is now regularly performed at 3 T or even 7 T, has caused researchers to reassess how DCE-MRI data should be acquired and analyzed.

ISSN 2379-1381 https://doi.org/10.18383/j.tom.2019.00015

This movement to higher fields affects DCE-MRI because, in addition to enhancing the longitudinal relaxation rate (R1), Gd-based contrast agents enhance transverse relaxation (R2*). While this is exploited in dynamic susceptibility contrast (DSC)-MRI, DCE-MRI data is acquired using heavily T1-weighted sequences and thus commonly assumed to be negligibly impacted by R2* relaxation. This assumption is less valid at high field than at low field because, in general, with increasing magnetic field strength, effective transverse relaxivity (r2*) tends to increase, while longitudinal relaxivity (r1) tends to decrease (10, 11). Hence, R2* correction is especially important for preclinical studies, which are often performed at a high-magnetic-field strength of 7 T or higher. But even in the clinic, there is a trend toward higher field strengths (12), which means that R2* correction may become more important in the future.

To address this problem, there is a growing use of multiecho sequences for both DCE-MRI (13, 14) and DSC-MRI (15, 16) to directly measure and account for contrast agent–induced R2* enhancement. Several clinical and preclinical studies conducted at various field strengths from 3 T to 7 T have investigated the effect of R2* relaxation on the accuracy of measuring contrast agent concentration in arterial blood (17, 18) and in the tissue of interest (19-21) and have shown that R2* can significantly affect quantitative DCE-MRI analysis (17-19, 21). However, the number of echoes required for reliable R2* correction and how the impact of R2* relaxation on DCE-MRI parameter estimation varies between cancer types have not yet been established. Hence, the clinical significance of R2* correction in DCE-MRI remains unclear.

The objective of this study is to address the time and tissue dependence of the R2* effect on DCE-MRI parameter quantification and its impact on cancer treatment monitoring. First, we look at how the number of echoes used influences the precision of R2* measurements. Then, we show that R2* is not linearly dependent on contrast agent concentration but varies with time and that the R2* dependence is different when comparing a subcutaneous tumor xenograft model and a transgenic prostate cancer model. Finally, we quantify the effect of R2* correction on the pharmacokinetic parameters K^{trans}, v_e and v_p, and illustrate how the effect of antiangiogenic treatment can be underestimated when R2* correction is neglected.

METHODOLOGY

Animal Models

All procedures and experiments involving animals were approved by the Norwegian Animal Research Authority (application ID 9194) and performed according to the European Convention for the Protection of Vertebrate Animals used for Experimental and other Scientific Purposes.

Eight female nude mice were injected subcutaneously in the hind limb with 5×10^6 TOV-21G human ovarian cancer cells (ATCC, Manassas, VA). Details of cell cultures and animal housing and handling can be found in Cebulla et al. (22) and Kim et al. (23), respectively. Tumors were allowed to grow for 2–3 weeks before starting MRI experiments. MRI-measured tumor volumes ranged from 55 to 203 mm^3 (median = 169 mm^3).

Transgenic adenocarcinoma of the mouse prostate (TRAMP) mice were bred in-house after obtaining a genetically modified breeder pair from the C57BL/6 background from The Jackson Laboratory, USA. Seven male mice were scanned when they were of age between 22 and 34 weeks. Well-differentiated adenocarcinoma commonly develops in the TRAMP model by age 18 weeks (24), with poorly differentiated tumors developing in ~20%–30% of mice in our colony (25). Here, none of the mice showed signs of large, poorly differentiated tumors on palpation or in the images.

MRI

The TOV-21G tumors were imaged in vivo on a 7 T BioSpec 70/20 Avance III system (Bruker BioSpin, Ettlingen, Germany) using an 86-mm transmit volume coil and a receive-only mouse brain surface array coil. The mice were anesthetized with isoflurane (~2% in 67% air/33% O_2, 0.6 L/min), and respiration rates were maintained at 60–70 breaths/min. A warm-air blower was used to keep the animals' body temperature at 37°C during scanning.

The TRAMP mice were imaged in vivo on a 7 T Pharmascan 70/16 Avance III system (Bruker BioSpin) using a 72-mm transmit volume coil and a 20-mm receive-only loop surface coil with a dedicated preamplifier. The mice were anesthetized with sevoflurane (~2.5% in O_2; 0.4 L/min), and respiration rates were maintained at 50–60 breaths/min. A hot-water circulation system was used to keep the animals' body temperature at 37°C during scanning.

To define tumor/prostate regions of interest (ROI), high-resolution T2-weighted (T2w) images were acquired using a rapid acquisition with relaxation enhancement sequence. To compute baseline R1 maps, images were acquired using a rapid acquisition with relaxation enhancement sequence with variable repetition times (VTR). For DCE-MRI, a dynamic series of images was acquired using a spoiled multiple-gradient echo sequence with 10 echo times (TE). After the 10th baseline image, a bolus of Gd-DOTA (Dotarem®, Guerbet, Villepinte, France) was manually injected via the tail vein within 4 seconds (during the 11th repetition) at a dose of 0.1 mmol/kg. Pulse sequence parameters are provided in Table 1.

Immediately after imaging, the TOV-21G tumor-bearing mice were treated with 5 mg/kg of bevacizumab (Avastin®, Genentech, South San Francisco, CA), administered intraperitoneally. Posttreatment scans using the same protocol were performed 2 days later. In a previous study, we showed that this regimen significantly reduced the blood volume, vascular density, and K^{trans} of TOV-21G tumors (26).

Image Analysis

TOV-21G tumor ROIs and TRAMP prostate ROIs were manually defined on the high-resolution T2w images and then downsampled to the resolution of the VTR and DCE-MRI images. For comparison with normal tissue, ROIs were drawn in the muscle adjacent to the TOV-21G tumors, and the same analysis was performed. For each voxel in the ROIs, a 3-parameter monoexponential decay model was fitted to the multiecho DCE-MRI data (all 10 echoes):

$$S(TE, t) = S_0(t)\exp(-R2^*(t)TE) + \varepsilon(t). \quad (1)$$

In addition, to examine the effect of TE on the R2* estimation, nonlinear regression and simple log-linear calculations

Table 1. Pulse Sequence Parameters

	TOV-21G			TRAMP		
	RARE (ROI)	VTR-RARE (T1 Map)	MGE (DCE-MRI)	RARE (ROI)	VTR-RARE (T1 Map)	MGE (DCE-MRI)
TE (ms)	60	10	1.8, 3.8, 5.8,. . .,19.8	36	6	1.7, 3.5, 5.3,. . ., 17.9
TR (ms)	2000	250, 500, 1000, 2000, 4000, 8000	118	5500	350, 600, 1000, 1500, 3000, 6000	220
RARE Factor	16	2	n/a	8	2	n/a
FA (°)	90	90	40	90	90	56
Matrix (Interpolated)	154 × 144 (192 × 192)	50 × 42 (50 × 50)	50 × 42 (50 × 50)	255 × 144 (255 × 192)	85 × 48 (85 × 64)	85 × 48 (85 × 64)
Averages	8	1	1	5	1	1
Temporal Resolution (s)	144	330	4.96	495	300	10.56
Repetitions	1	1	200	1	1	100
FOV (mm)	14 × 14			25.5 × 19.2		
Slices	5			23	9	9
Slice Thickness/Slice Gap (mm)	0.8/0.2			0.66/0		

Abbreviations: TOV-21G, human ovarian cancer xenograft model; TRAMP, transgenic adenocarcinoma of the mouse prostate; RARE, rapid acquisition with relaxation enhancement; ROI, region of interest; TR, repetition time; VTR, variable TR; T1, longitudinal relaxation time; MGE, multiple-gradient echo; DCE-MRI, dynamic contrast-enhanced magnetic resonance imaging; TE, echo time; FA, flip angle; FOV, field of view.

were performed using the first 5 echoes and the first 2 echoes, respectively. Voxels for which the median R^2 or the minimum R^2 over the whole time-course was <0.75 or 0.5, respectively, were excluded from further analysis.

DCE-MRI analysis was performed using either the first echo signal only, which is equivalent to standard single-echo DCE-MRI (uncorrected), or the model-estimated $S(TE = 0, t) = S_0(t) + \varepsilon(t)$ to account for R2* relaxation (R2*-corrected). The measured (uncorrected) and estimated (R2*-corrected) signal–time curves were converted to uncorrected and R2*-corrected Gd-DOTA concentration–time curves by using the baseline R1 ($R1_0$) maps computed from the VTR data and by assuming a linear relation-

Table 2. Precision of R2* Estimation as a Function of Number of Echoes

	R2* Coefficient of Determination		Baseline R2* Coefficient of Variation		
TOV-21G	5-Echo	10-Echo	2-Echo	5-Echo	10-Echo
1	0.955 [0.900 0.981]	0.971 [0.949 0.983]	0.618 [0.390 1.002]	0.164 [0.114 0.233]	0.083 [0.056 0.114]
2	0.966 [0.917 0.987]	0.974 [0.953 0.987]	0.446 [0.254 0.763]	0.138 [0.093 0.204]	0.084 [0.055 0.117]
3	0.956 [0.901 0.982]	0.968 [0.944 0.983]	0.731 [0.449 1.265]	0.171 [0.110 0.257]	0.073 [0.047 0.109]
4	0.964 [0.920 0.985]	0.976 [0.959 0.987]	0.499 [0.324 0.771]	0.127 [0.092 0.180]	0.059 [0.044 0.080]
5	0.955 [0.906 0.980]	0.968 [0.948 0.981]	0.669 [0.437 1.047]	0.167 [0.110 0.239]	0.073 [0.048 0.103]
6	0.961 [0.906 0.985]	0.971 [0.950 0.984]	0.659 [0.362 1.098]	0.179 [0.107 0.268]	0.091 [0.057 0.133]
7	0.964 [0.917 0.986]	0.972 [0.951 0.985]	0.595 [0.343 1.068]	0.153 [0.099 0.235]	0.074 [0.050 0.105]
8	0.975 [0.944 0.989]	0.976 [0.960 0.986]	0.436 [0.286 0.717]	0.116 [0.080 0.165]	0.053 [0.036 0.070]
TRAMP					
1	0.906 [0.787 0.958]	0.933 [0.887 0.961]	1.124 [0.726 1.962]	0.277 [0.200 0.372]	0.114 [0.086 0.154]
2	0.842 [0.631 0.934]	0.903 [0.827 0.944]	1.537 [0.967 2.755]	0.412 [0.311 0.576]	0.184 [0.137 0.244]
3	0.865 [0.698 0.941]	0.914 [0.849 0.950]	1.286 [0.838 2.213]	0.320 [0.239 0.419]	0.135 [0.104 0.173]
4	0.767 [0.432 0.913]	0.859 [0.733 0.926]	1.766 [1.073 3.409]	0.590 [0.391 1.993]	0.260 [0.182 0.369]
5	0.745 [0.377 0.903]	0.859 [0.723 0.925]	1.556 [0.931 2.952]	0.450 [0.331 0.742]	0.214 [0.151 0.297]
6	0.762 [0.392 0.912]	0.865 [0.729 0.931]	1.878 [1.121 3.744]	0.532 [0.370 1.989]	0.250 [0.172 0.358]
7	0.873 [0.710 0.944]	0.920 [0.863 0.953]	1.562 [0.870 3.257]	0.269 [0.181 0.391]	0.111 [0.078 0.156]

Median values and [25th and 75th percentiles] are reported for each animal.

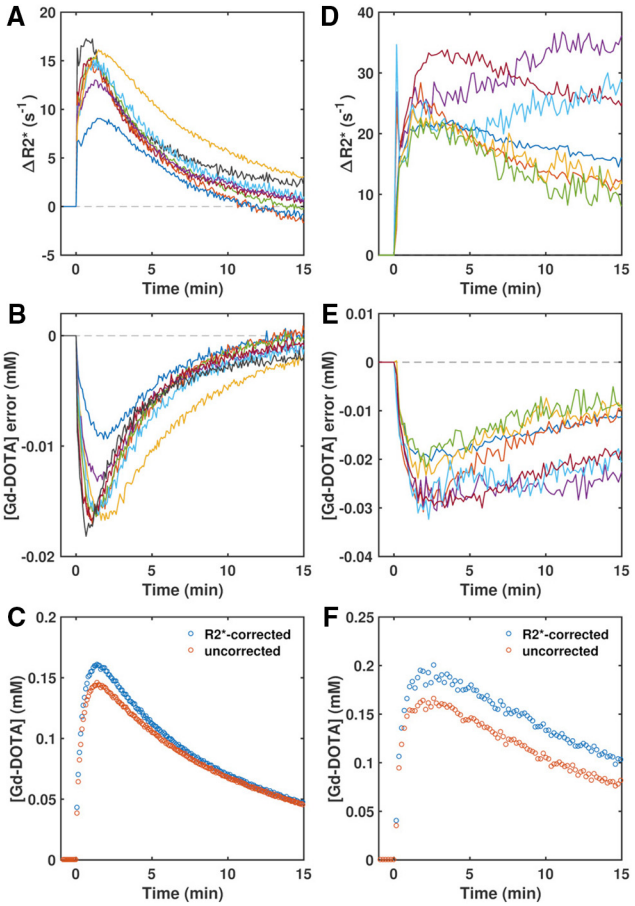

Figure 1. R2* enhancement causes underestimation of Gd-DOTA concentration. Median ΔR2*–time curve (R2* enhancement relative to the median baseline value) for each TOV-21G ovarian tumor xenograft (A) and transgenic adenocarcinoma of the mouse prostate (TRAMP) prostate (D). Corresponding median errors in Gd-DOTA contrast agent concentration if calculated without correcting for R2* relaxation (B and E). Median uncorrected and R2*-corrected concentration–time curves for an example TOV-21G tumor (C) and TRAMP prostate (F).

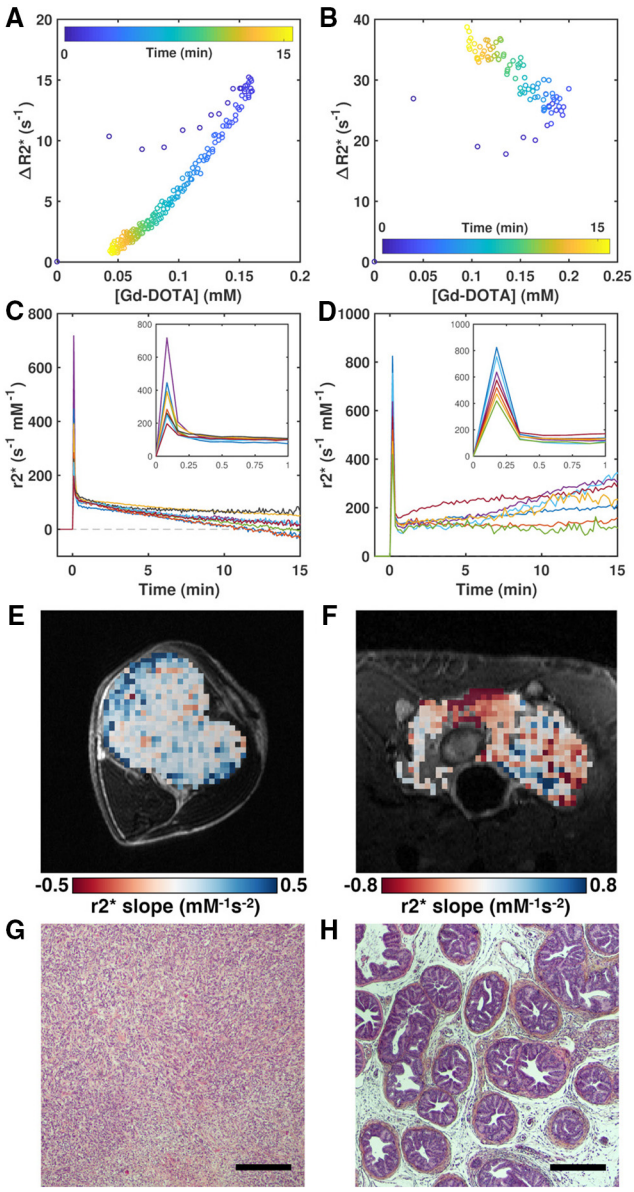

Figure 2. Gd-DOTA r2* relaxivity varies with time and tissue type. Plots of median ΔR2* (relative to the median baseline value) versus median Gd-DOTA concentration parameterized by time for the same TOV-21G ovarian tumor xenograft (A) and TRAMP mouse prostate (B) in Figure 1, C and F. Median r2* relaxivity–time curve (r2* = ΔR2*/[Gd-DOTA]) for each TOV-21G tumor (C) and TRAMP prostate (D). Map of the r2* slope from 30 seconds after Gd-DOTA administration to the final time point for an example TOV-21G tumor (E) and TRAMP prostate (F). Images of hematoxylin–eosin–saffron (HES)-stained sections illustrating the vastly different tissue architectures of a TOV-21G tumor (G) and a TRAMP prostate (H). Scale bars = 300 μm.

ship between R1 and concentration and a constant r1 of 3.2 $mM^{-1}\ s^{-1}$ (27):

$$[\text{Gd-DOTA}](t) = (R1(t) - R1_0)/r1 \qquad (2)$$

Maps of the dynamic effective transverse relaxivity r2* of Gd-DOTA were estimated assuming an analogous relationship:

$$r2^*(t) = (R2^*(t) - R2^*_0)/[\text{Gd-DOTA}](t) \qquad (3)$$

A biexponential arterial input function (AIF) was used for pharmacokinetic (PK) modeling:

$$C_p(t) = D(A_1 \exp(-m_1 t) + A_2 \exp(-m_2 t)) \qquad (4)$$

where D is the administered contrast agent dose (here 0.1 mmol/kg), A_1 = 11.27 kg/L, m_1 = 0.8 min^{-1}, A_2 = 4.23 kg/L, and m_2 =

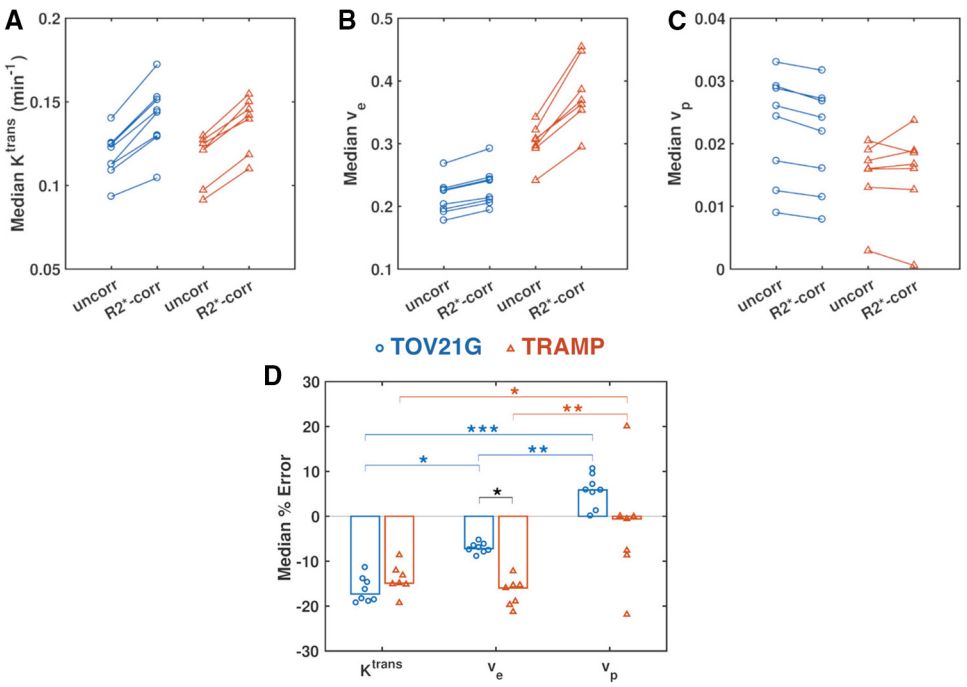

Figure 3. R2* enhancement affects accuracy of dynamic contrast-enhanced magnetic resonance imaging (DCE-MRI) parameters. Median K^{trans} (A), v_e (B), and v_p (C) values without (uncorr) and with correction for R2* relaxation (R2*-corr) for each TOV-21G ovarian tumor xenograft (blue circles) and TRAMP mouse prostate (red triangles). Paired *t* tests were performed to compare uncorrected and R2*-corrected values, and *P* values were corrected for multiple comparisons using the Benjamini–Hochberg procedure. Median percent errors (uncorrected vs R2*-corrected) of Tofts parameter estimates (D). A 2-way ANOVA and Tukey honest significant difference post hoc tests were performed to compare the errors in different parameters in different tissues (*$P < .05$, **$P < .001$, ***$P < .0001$).

0.0655 min^{-1}. These coefficient values were determined by empirically combining components of 2 population-averaged AIFs from the literature. The peak amplitude ($A_1 + A_2$) and m_1 were taken from a previous study that used similar manual bolus administration and contrast agent concentration and dose, but Gd-DTPA-BMA instead of Gd-DOTA (28). To account for the difference in the clearance kinetics of the different contrast agents, A_2 and m_2 were taken from another study that used Gd-DOTA (13). This hybrid AIF gave better model fits than either of the separate AIFs (see online supplemental Figure 1).

The extended Tofts model (29) was fitted to the uncorrected and R2*-corrected concentration-time curves using constrained ($0 \le K^{trans} \le 10, 0 \le v_e \le 1, 0 \le v_p \le 1$) nonlinear least-squares optimization to obtain uncorrected and R2*-corrected estimates of K^{trans}, v_e, and v_p. Voxels for which $R^2 < 0.5$ were excluded from further analysis. Voxels were classified as enhancing or nonenhancing using Otsu's method to threshold the relative signal enhancement images 60 s after contrast agent arrival. Nonenhancing voxels were also excluded from further analysis (see online supplemental Table 1).

Statistical Analysis

The coefficient of determination (R^2) was calculated for the monoexponential fits of the first 5 and all 10 echoes for each voxel and each acquisition time as a measure of goodness of fit.

The coefficient of variation of the 10 baseline R2* estimates was calculated for each voxel. Assuming a temporally constant baseline R2*, the coefficient of variation provides a measure of the precision of estimating R2* using the first 2, first 5, and all 10 echoes.

A 2-way analysis of variance was performed to determine if the effect of R2* on Tofts PK analysis (percent error in uncorrected parameter values with respect to R2*-corrected values) varies with the Tofts parameter (K^{trans}, v_e, v_p) and tissue type (TOV-21G, TRAMP). Tukey honest significant difference post hoc tests were performed on relevant pairs of parameters.

To assess the influence of the R2* effect on DCE-MRI-measured response to bevacizumab treatment in TOV-21G tumors, univariate paired *t* tests were performed on the pre- to posttreatment changes in uncorrected vs R2*-corrected Tofts parameter values. Paired *t* tests were also used to compare median percent errors in Tofts parameter values before and after treatment. The Benjamini–Hochberg procedure was used to correct for multiple testing.

RESULTS

More Echoes Give Better R2* Estimates

The R^2 of the R2* exponential decay model [equation (1)] was significantly greater ($P < .001$ for all animals, paired *t* test) when all 10 echoes were used than when only 5 echoes were used. However, the differences in median R^2 were small for the TOV-21G tumors, ranging from 0.08% to 1.7% (Table 2). The R^2 for the TRAMP prostates was low, and the differences between 5- and 10-echo median R^2 were large (3.0%–15.3%).

More importantly, the precision of R2* estimates, as measured by the coefficient of variation of the 10 baseline R2*

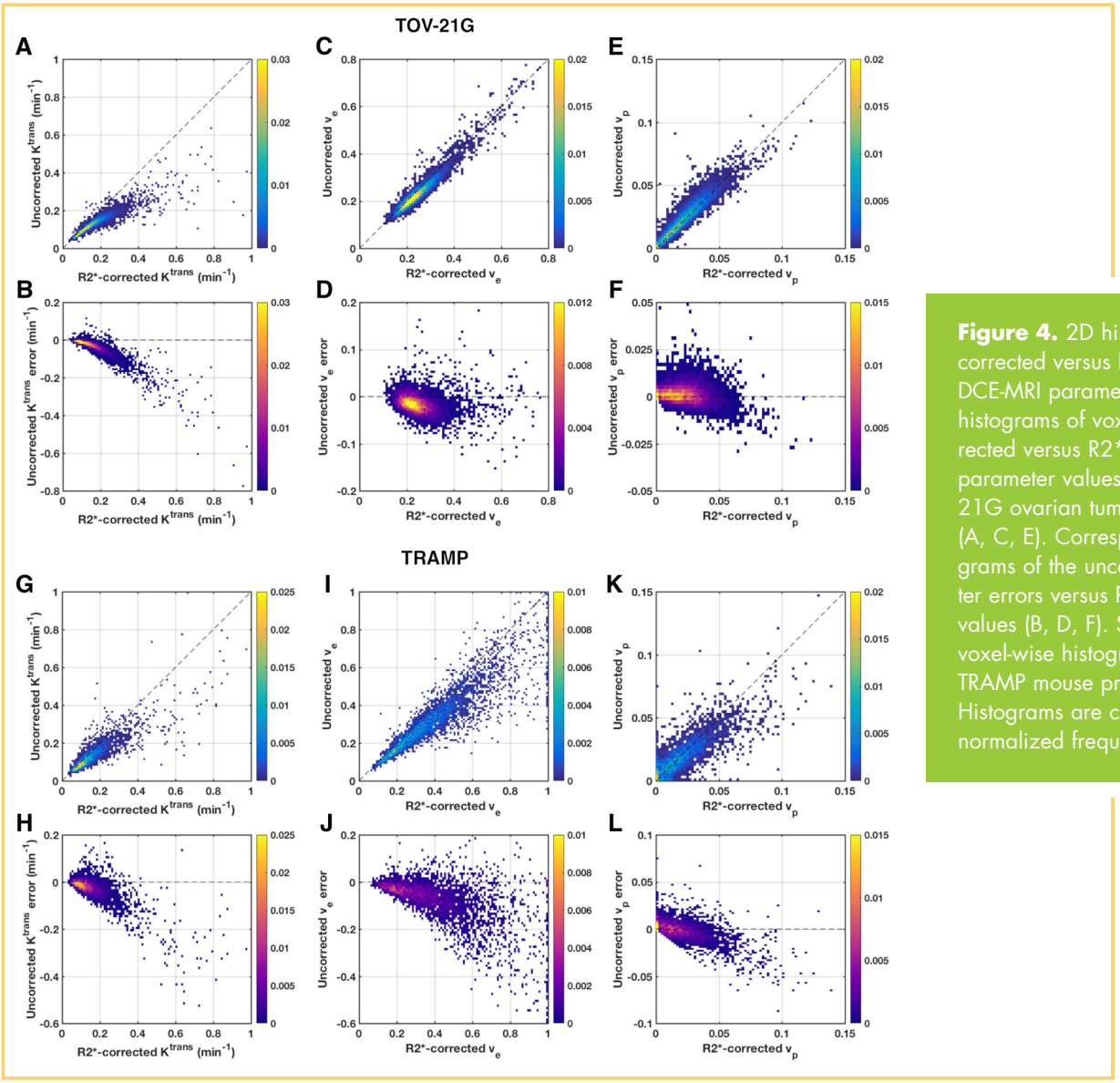

Figure 4. 2D histograms of uncorrected versus R2*-corrected DCE-MRI parameters. Pooled 2D histograms of voxel-wise uncorrected versus R2*-corrected Tofts parameter values from all TOV-21G ovarian tumor xenografts (A, C, E). Corresponding histograms of the uncorrected parameter errors versus R2*-corrected values (B, D, F). Similar pooled, voxel-wise histograms from all TRAMP mouse prostates (G-L). Histograms are color-coded by normalized frequency.

values, greatly increased with increasing number of echoes (Table 2). For the TOV-21G tumors, the median coefficients of variation were greater for 2-echo and 5-echo R2* estimates, by 5.3–10 times and 1.6–2.4 times, respectively, than for 10-echo estimates. For the TRAMP prostates, the 2-echo and 5-echo median coefficients of variation were 6.8–14 times and 2.1–2.4 times greater, respectively.

The absolute values of R2* were underestimated for high values of R2* for 2-echo estimates compared to 10-echo estimates, but the spread in 2-echo estimates was relatively low (see online supplemental Figure 2A). For low values of 10-echo R2* estimates, the spread in 2-echo R2* estimates was high, particularly for the TRAMP prostates. Compared with the 2-echo estimates, the 5-echo R2* estimates were in better agreement with the 10-echo R2* estimates.

R2* Enhancement Causes Underestimation of Gd-DOTA Concentration

In TOV-21G tumors, R2*–time curves followed the general shape of Gd-DOTA concentration–time curves—rapid initial enhancement followed by a slower return toward baseline (Figure 1A). This dynamic R2* enhancement resulted in a time-dependent underestimation of the Gd-DOTA tissue concentration if the R2* decay was not accounted for, with the error peaking at peak concentration and then decreasing throughout the washout phase (Figure 1, B and C). The median contrast agent concentration error within each tumor ROI ranged from −9.4% to −16% at peak concentration and from −6.1% to +2.6% at the end of the time series.

In comparison, the TRAMP prostates exhibited greater initial enhancement and slower subsequent decrease in R2*; in 2 TRAMPs, R2* actually continued to increase during washout (Figure 1, D and F). Compared to TOV-21G tumors, in TRAMP prostates, the greater and more prolonged R2* enhancement resulted in greater concentration errors across the time course (Figure 1E). The ROI-median contrast agent concentrations were underestimated by between 13% and 20% at peak concentration and between 14% and 29% at the end of the time series.

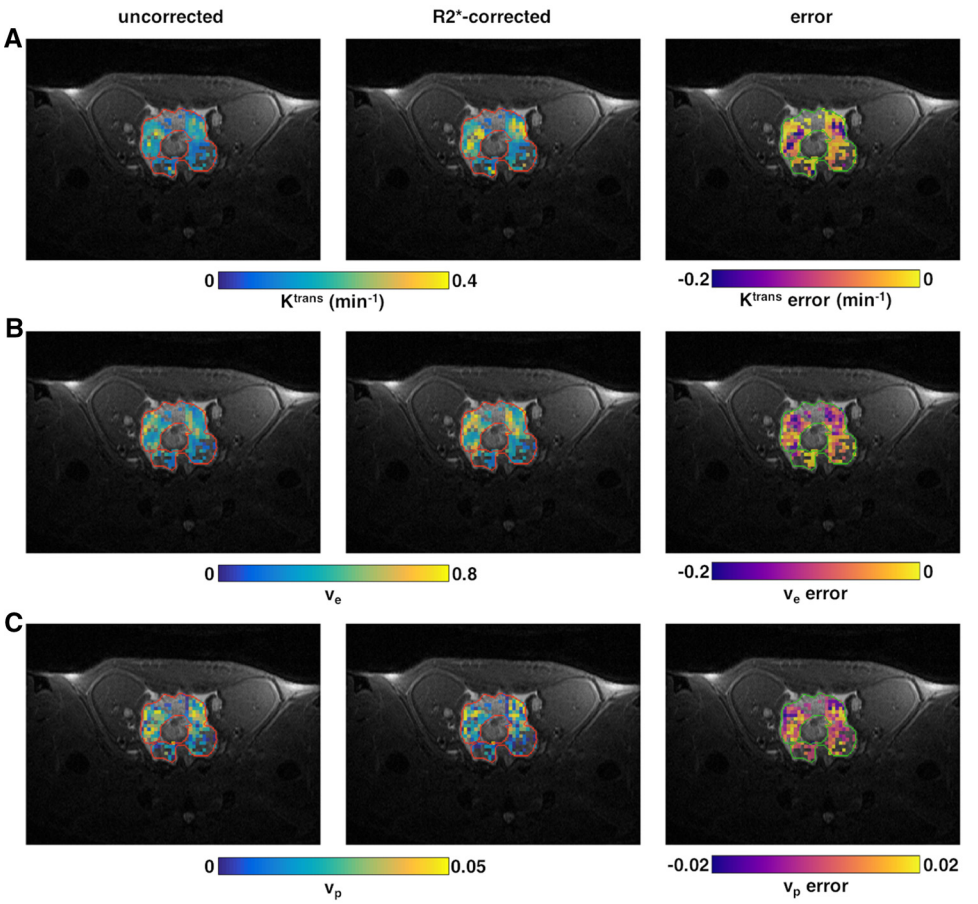

Figure 5. DCE-MRI parametric maps for a TRAMP prostate. Maps of K^{trans} (A), v_e (B), and v_p (C). Each panel shows maps of the uncorrected values (left column), R2*-corrected values (center column), and the error (right column). Maps are overlaid on the high-resolution T2-weighted (T2w) anatomical image. Nonenhancing voxels and voxels where R2* or Tofts model fitting were poor [R2* median $R^2(t) < 0.75$ or R2* minimum $R^2(t) < 0.5$ or Tofts $R^2 < 0.5$] are not shown on the maps.

Gd-DOTA r2* Relaxivity Varies With Time and Tissue Type

Although Gd-DOTA concentration, R2* enhancement, and concentration error were interrelated as expected, the relationships were not simply linear, that is, the effective r2* relaxivity of the contrast agent was not constant. The time-varying r2* is illustrated in plots of R2* enhancement ($\Delta R2^*$) versus Gd-DOTA concentration for an example TOV-21G tumor and TRAMP prostate (Figure 2, A and B). There were 2 "branches" to these curves, one corresponding to the initial intravascular/wash-in phase (increase in Gd concentration with time) and the other to the later extravascular/washout phase (decrease in Gd concentration with time).

In both animal models, the initial r2* relaxivity was very high when the contrast agent was presumably still mostly contained in the vasculature (Figure 2, C and D). The ROI-median initial r2* ranged from 197 to 717 $s^{-1}mM^{-1}$ in TOV-21G tumors and from 419 to 825 $s^{-1}mM^{-1}$ in TRAMP prostates. Subsequently, r2* rapidly decreased after the first pass of the bolus and as the contrast agent ostensibly extravasated into the tissue. After this, the r2* behavior diverged in the 2 cancer models—on average, r2* slowly decreased with time in the TOV-21G tumors, but it slowly increased with time in the TRAMP prostates. This difference between the 2 tissues is illustrated in Figure 2, E and F, which shows maps of the r2* slope calculated from 30 seconds post injection to the final time point. The r2* slope was generally flat or negative in the TOV-21G tumor, whereas it was positive in large areas of the TRAMP prostate.

R2* Enhancement Affects Accuracy of DCE-MRI Parameters

The underestimation of Gd-DOTA concentration owing to R2* enhancement led to errors in PK modeling (ie, differences between uncorrected and R2*-corrected parameter values; Figures 3–6). Furthermore, the time- and tissue-dependence of r2* resulted in different effects on each Tofts parameter and on each tissue type ($P < .05$, 2-way ANOVA; Table 3).

K^{trans} was underestimated in both TOV-21G tumors and TRAMP prostates, with the median percent error of uncorrected versus R2*-corrected values ranging from 11% to 19% and 8.6% to 19%, respectively (Figure 3, A and D). The K^{trans} error was not significantly different between the cancer models ($P = .963$; Table 4).

V_e was underestimated in TOV-21G tumors by 5.3% to 8.9%, which was significantly less than the 12% to 21% underestimation of v_e in the TRAMP prostates ($P = .019$; Table 4, Figure 3, B and D). In the TOV-21G tumors, R2* enhancement affected K^{trans} measurements significantly more than v_e measurements ($P = .024$); but in the TRAMP prostates, the effects of R2* enhancement on K^{trans} and v_e were comparable ($P = .924$).

Interestingly, R2* enhancement resulted in overestimation of v_p in the TOV-21G tumors. There was a large variance in v_p errors (−22% to +20%) in the TRAMP prostates (Figure 3, C and D).

Not only did Gd-DOTA-induced R2* enhancement have different effects on different parameters in different tissue types, the effect was not constant for a given parameter and tissue type (Figure 4). This was most apparent with TOV-21G K^{trans}, for

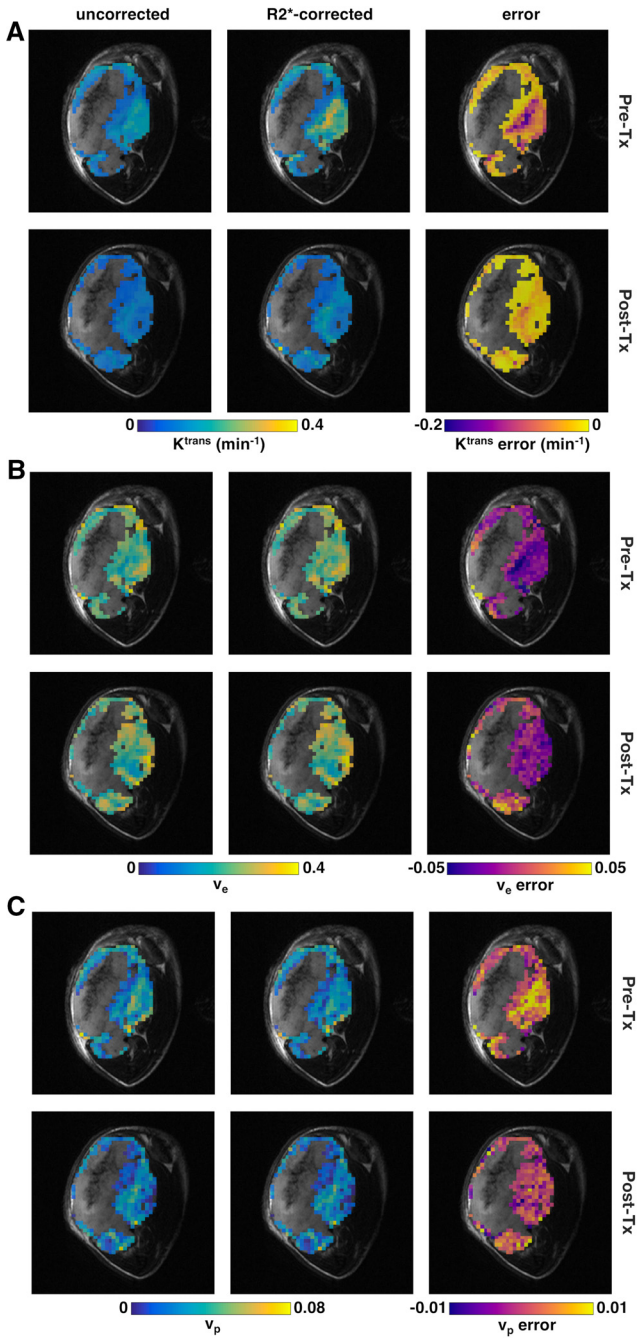

Figure 6. DCE-MRI parametric maps for a TOV-21G ovarian tumor xenograft. Maps of K^{trans} (A), v_e (B), and v_p (C). Each panel shows maps of the uncorrected values (left column), R2*-corrected values (center column), and the error (right column) before (top row) and 48 hours after (bottom row) bevacizumab treatment (5 mg/kg). Maps are overlaid on the high-resolution T2w anatomical image. Nonenhancing voxels and voxels where R2* or Tofts model fitting were poor [R2* median $R^2(t) < 0.75$ or R2* minimum $R^2(t) < 0.5$ or Tofts $R^2 < 0.5$] are not shown on the maps.

which there was a clear nonlinear relationship between the uncorrected and R2*-corrected values (Figure 4, A and B). The error was relatively small for low K^{trans}, but it grew increasingly larger for higher K^{trans}. Similar trends were seen to lesser degrees for K^{trans} and v_e in TRAMP prostates (Figure 4, G–J). As mentioned above, the median v_p was overestimated in every TOV-21G tumor; on the voxel level, for both TOV-21G and TRAMP, overestimation occurred mostly for small v_p (< 0.05), and underestimation was more common for larger v_p (Figure, 4, E–F and K–L).

The number of echoes used for R2* correction also influenced the DCE-MRI parameters (see online supplemental Figure 2, B–D). For the TOV-21G tumors, the 5-echo R2*-corrected parameters approximated the 10-echo R2*-corrected ones fairly well. However, high K^{trans} were underestimated when only 2 or 5 echoes were used in comparison to 10 echoes. For the TRAMP prostates, the differences between 5-echo and 10-echo R2*-corrected parameters were larger than those for the TOV-21G tumors.

R2* Enhancement Diminishes DCE-MRI-Measured Treatment Effect Size

Median K^{trans} was significantly reduced ($P < .001$ for both uncorrected and R2*-corrected K^{trans}) in the TOV-21G tumors 48 hours after treatment with bevacizumab (Figures 6 and 7). Median v_e and v_p were also reduced to a lesser extent (uncorrected $P = .086$ and 0.075, respectively; R2*-corrected $P = .070$ and 0.086, respectively).

The magnitude of the treatment-induced reduction in K^{trans} was underestimated when R2* was not accounted for. This is especially apparent when looking at the right tail of the pooled histogram of all eligible voxels (based on the goodness of fit and initial enhancement thresholds) from all tumor ROIs (Figure 7A). The R2*-corrected 95th percentile K^{trans} decreased by 0.127 ± 0.042 min^{-1} (mean ± SD) after treatment, but the uncorrected 95th percentile K^{trans} decreased by only 0.065 ± 0.27 min^{-1}. Thus, the uncorrected treatment effect size (Cohen's $d_z = -2.45$) was less than the R2*-corrected effect size ($d_z = -3.07$). This was mainly owing to the underestimation of the high K^{trans} values before treatment. The median K^{trans} was less affected by R2* relaxation, and subsequently, the treatment effect on median K^{trans} was underestimated to a lesser degree—the reduction in R2*-corrected and uncorrected median K^{trans} was 0.051 ± 0.015 min^{-1} ($d_z = -3.36$) and 0.037 ± 0.012 min^{-1} ($d_z = -3.12$), respectively. Importantly, the treatment-induced changes in both median and 95th percentile K^{trans} were greater after R2* correction in each individual tumor (Figure 7B).

Compared with K^{trans}, v_e and v_p were less affected by bevacizumab treatment, and the treatment effect sizes were less affected by R2* relaxation. For all 3 Tofts parameters, the magnitude of the median percent error in parameter measurements owing to R2* enhancement decreased after treatment (Figure 7C).

In the muscle, absolute K^{trans}, v_e and v_p were lower and the errors in uncorrected parameter estimates were smaller compared with highly perfused areas of the tumor tissue and TRAMP prostates (see online supplemental Figure 3). Changes in DCE-parameters from before to after treatment were much lower in

Table 3. Results of 2-Way ANOVA Comparing R2* Effects Across Tissue Types and Tofts Parameters

Source	Sum of Squares	df	Mean Square	*F*-Statistic	*P*-Value
Tissue Type[a]	312.909	1	312.909	9.800	.003
Parameter[b]	2360.776	2	1180.388	36.968	<.001
Tissue Type × Parameter	333.915	2	166.958	5.229	.010
Error	1245.272	39	31.930		
Total	4331.291	44			

Abbreviation: df, degrees of freedom.
[a]Tissue types, TOV-21G tumor and TRAMP prostate.
[b]Parameters: K^{trans}, v_e, and v_p.

the muscle than in the tumor tissue and TRAMP prostates (see online supplemental Figure 3).

DISCUSSION

Here, we showed that pharmacokinetic modeling of DCE-MRI data is influenced by R2* relaxation, which is in agreement with previous studies (17, 19).

One of the aims of the study was to investigate how many echoes are necessary to provide reliable R2* estimates. We showed that using more echoes for estimating R2* resulted in higher R2* precision. However, the number of echoes necessary for R2* correction depends on the study. A trade-off needs to be made between the number of echoes and the temporal and spatial resolution of the MR images. Although a high temporal resolution allows for better PK modelling, a higher number of echoes results in more accurate and precise R2* correction. When the signal-to-noise ratio and image quality are good, 5 or even 2 echoes may be sufficient. In this study, the TRAMP prostates required a higher number of echoes for accurate R2* computation than the TOV-21G tumors. This is likely because of noise from flow and motion artifacts that were particularly conspicuous in mice with full bladders as the contrast agent flowed into the bladders over time. The artifacts and lower temporal resolution (owing to the larger number of slices required to cover the tissue of interest) in the TRAMP data resulted in poorer R2* and PK model fitting (see online supplemental Table 1). These and other differences in data acquisition (scanners, radiofrequency coils, pulse sequence parameters [Table 1]) confound direct comparisons between the TRAMP and TOV-21G results.

Despite this, one very interesting finding of our study was that the time dependence of R2* enhancement and r2* differed in the 2 cancer models. In both models, an initial spike in R2* and r2*, which corresponds to the first pass of the contrast agent bolus, was observed. Then, the TOV-21G xenograft data behaved as expected, with R2* increasing and then decreasing as the contrast agent extravasated from the blood vessels and was cleared from the tumor tissue. During the washout phase, r2* slowly decreased over time in the TOV-21G tumors. This indicates that field inhomogeneities were reduced, as the Gd was distributed throughout the extravascular–extracellular space of the macroscopically homogeneous tumor tissue (Figure 2G). In a few tumors, negative r2* values were measured at late time points (Figure 2C). It has been shown through simulations and phantom experiments that R2* is a nonmonotonic (quadratic) function of contrast agent concentration and that this nonmonotonicity increases with field strength (30). It is possible that R2* decreases below the baseline values at low contrast agent concentration and compartmentalization. This may explain the observed negative r2*.

Table 4. Post Hoc Comparisons of R2* Effects Between Tissue Types and Tofts Parameters Using Tukey Honest Significant Difference Tests

Parameter Pair	Lower 95% CI	Estimated Difference	Upper 95% CI	*P*-Value
TOV-21G–TRAMP K^{trans}	−11.150	−2.388	6.374	0.963
TOV-21G–TRAMP v_e[a]	**1.106**	**9.868**	**18.630**	**0.019**
TOV-21G–TRAMP v_p	−0.384	8.377	17.139	0.068
TOV-21G K^{trans}–v_e	**−17.783**	**−9.319**	**−0.854**	**0.024**
TOV-21G K^{trans}–v_p	**−30.592**	**−22.127**	**−13.663**	**<0.001**
TOV-21G v_e–v_p	**−21.273**	**−12.809**	**−4.344**	**0.001**
TRAMP K^{trans}–v_e	−6.112	2.937	11.986	0.924
TRAMP K^{trans}–v_p	**−20.411**	**−11.362**	**−2.313**	**0.007**
TRAMP v_e–v_p	**−23.348**	**−14.299**	**−5.250**	**0.000**

Abbreviation: CI, confidence interval.
[a]Significant differences ($P < .05$) are highlighted in bold.

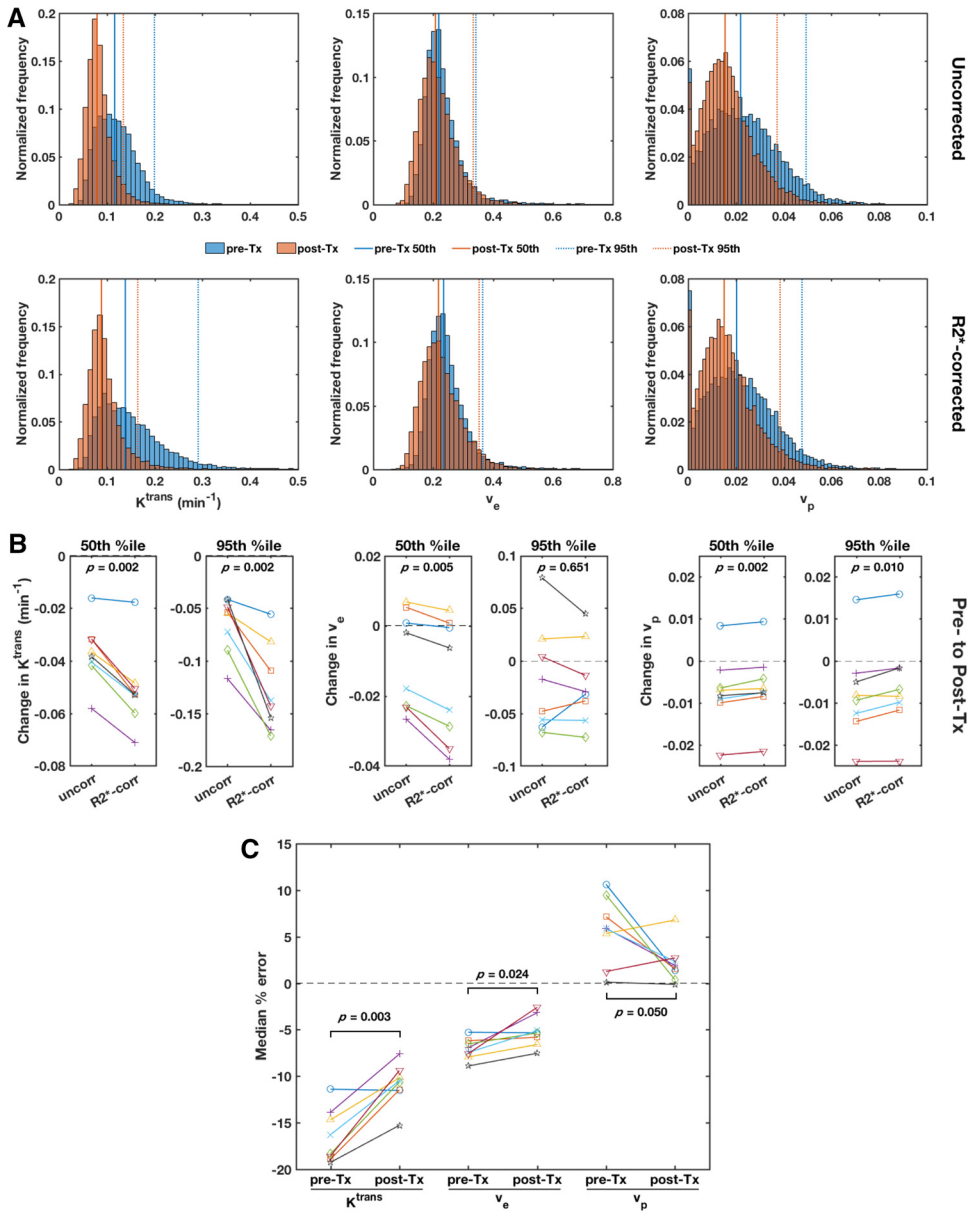

Figure 7. R2* enhancement diminishes DCE-MRI-measured treatment effect size. Pooled histograms of voxel-wise uncorrected (top row) and R2*-corrected (bottom row) Tofts parameter values (left to right: K^{trans}, v_e, v_p) from all TOV-21G ovarian tumor xenografts before (pre-Tx, blue) and 48 h after bevacizumab treatment (post-Tx, red) (A). The solid vertical lines mark the pre- and post-Tx medians, and the dotted vertical lines mark the pre- and post-Tx 95th percentiles. The treatment-induced changes in median (50th %tile) and 95th percentile uncorrected and R2*-corrected Tofts parameter values for each tumor (B). Paired *t* tests were performed to compare uncorrected and R2*-corrected changes, and *P* values were corrected for multiple comparisons using the Benjamini–Hochberg procedure. The median voxel-wise percent errors in uncorrected Tofts parameter estimates compared with R2*-corrected estimates for each tumor pre- and post-Tx (C). Paired *t* tests were performed to compare the pre- and post-Tx errors, and *P* values were corrected for multiple comparisons using the Benjamini–Hochberg procedure.

Interestingly, the R2* and r2* behaved very differently in the TRAMP prostates. After the initial peak, R2* decreased much more slowly or even continued to increase during the washout phase, corresponding to stable or increasing r2*. This could be explained by the extravasated contrast agent becoming recompartmentalized in and around the glandular structures of the prostate and increasing field heterogeneity (Figure 2H). While the exact reasons for this divergent R2* behavior cannot be elucidated here, it is important to note that the tissue structure can play an important role in the contrast agent distribution and the time dependence of r2* (31, 32). Thus, it would be difficult to correct for R2* enhancement *a priori*.

In this study, we show that the uncorrected DCE-MRI parameters K^{trans} and v_e were significantly underestimated, which is in line with previous studies (19, 21). Zhang et al. reported median percent errors of larger than 20% for both K^{trans} and v_e at 7 T (19), which is slightly larger than what we saw in our study. Heilmann et al. also reported a significant underestimation of K^{trans} and slight underestimation of v_e at 4.7 T (for R2* correction of both AIF and concentration–time curve) (21). The greater the K^{trans} or v_e and v_p, the greater was their underestimation without R2* correction. Our results also confirm the findings of Zhang et al. that the error without R2* correction increased for greater parameter values (19). Similar to our study, the errors were particularly high for high K^{trans} values, which suggests that R2* correction is particularly important for tissues with high K^{trans}. Importantly, we found that the relationship between corrected and uncorrected DCE-MRI parameters was not linear, especially in K^{trans} in the TOV-21G tumors. The disproportionately large errors in regions of high K^{trans} can lead to underestimation of tumor heterogeneity (Figure 6A), which is an important, clinically relevant prognostic factor (33). In less

perfused tissue such as muscle, R2* correction plays a less important role.

In cancer treatment, response to chemotherapy and antivascular therapies is often associated with a decrease in K^{trans} from baseline (34, 35). An important finding in our study was that the therapeutic effect can be underestimated when non-R2*-corrected DCE-MRI parameters are used for treatment monitoring. Underestimation of treatment effect will be particularly large for tumors or tumor regions with high K^{trans}. This is significant because a previous study conducted at 1.5 T has shown that changes of around 44% for Ktrans and 41% for v_e may be necessary to indicate a treatment effect due to a relatively high uncertainly of K^{trans} in repeatability measurements (36). At higher field strengths, R2* enhancement may further increase uncertainty in DCE-MRI measurements, and correcting for it would improve their reliability as biomarkers of treatment response.

A limitation of this study was the use of a population-averaged AIF from the literature. While individual AIFs might provide more accurate DCE-MRI results, they are challenging to acquire, and it has been shown that there is a high correlation between DCE-MRI parameters derived using individual and population-based AIFs (37). Previous studies have shown that it is important to perform R2* correction on the AIFs, as noncorrected AIFs have been shown to overestimate K^{trans} (17–19). Hence, the use of R2*-corrected AIFs may have diminished the underestimation of K^{trans} reported here (19). In contrast, the AIF obtained in our study was derived from 2 studies that measured plasma Gd concentrations with MRI at 2.35 T (28) and with mass spectrometry (13) and was thus less affected by R2* relaxation.

In conclusion, we showed that the R2* enhancement in DCE-MRI is both time- and tissue-dependent. Furthermore, our results suggest that R2* enhancement may significantly impact pharmacokinetic analysis. As expected, acquiring more echoes allows more accurate and precise measurement of R2*, but the trade-off between better R2* estimation and higher temporal resolution should be considered. In particular in tissue with high K^{trans}, R2* correction should be performed to avoid underestimation. This has consequences for the use of K^{trans} and other DCE-MRI parameters as biomarkers in cancer diagnosis, because underestimation of K^{trans} can mislead prognosis and evaluation of treatment response if R2* enhancement is neglected.

Supplemental Materials

Supplemental Figure 1: https://doi.org/10.18383/j.tom.2019.00015.sup.01

Supplemental Figure 2: https://doi.org/10.18383/j.tom.2019.00015.sup.02

Supplemental Figure 3: https://doi.org/10.18383/j.tom.2019.00015.sup.03

Supplemental Table 1: https://doi.org/10.18383/j.tom.2019.00015.sup.04

ACKNOWLEDGMENTS

Contract grant sponsor: The liaison committee between the Central Norway Regional Health Authority (RHA) and the Norwegian University of Science and Technology (NTNU); contract grant number: 90059700; contract grant number: 46056806. And the Norwegian Cancer Society; contract grant number 6824920-2015.

We thank Sonja Andersen and Kristine Pettersen (NTNU) for growing the TOV21G cells.

Animals were housed in the Comparative Medicine Core Facility (NTNU) and in the animal facility of the University of Bergen (UiB). We thank, especially, Nils Hagen for breeding the TRAMP mice, as well as Anne Åm and Trine Skoglund (NTNU) and Aurora Brønstad and Gry Bernes (UiB) for logistics.

In vivo MRI was performed at the MR Core Facility (NTNU) and the Molecular Imaging Center (UiB). We thank Frits Thorsen (UiB) for assistance with scanning.

Histology was performed at the Cellular & Molecular Imaging Core Facility (NTNU); we thank Ingunn Nervik.

Disclosures: No disclosures to report.

Conflict of Interest: None reported.

REFERENCES

1. Türkbey B, Thomasson D, Pang Y, Bernardo M, Choyke PL. The role of dynamic contrast-enhanced MRI in cancer diagnosis and treatment. Diagn Interv Radiol. 2010;16:186–192.
2. Heye AK, Culling RD, Valdés Hernández Mdel C, Thrippleton MJ, Wardlaw JM. Assessment of blood-brain barrier disruption using dynamic contrast-enhanced MRI. A systematic review. Neuroimage Clin. 2014;6:262–274.
3. Tofts PS, Kermode AG. Measurement of the blood-brain barrier permeability and leakage space using dynamic MR imaging. 1. Fundamental concepts. Magn Reson Med. 1991;17:357–367.
4. Pelgrim GJ, Handayani A, Dijkstra H, Prakken NH, Slart RH, Oudkerk M, Van Ooijen PM, Vliegenthart R, Sijens PE. Quantitative myocardial perfusion with dynamic contrast-enhanced imaging in MRI and CT: theoretical models and current implementation. Biomed Res Int. 2016;2016:1734190.
5. Gordon Y, Partovi S, Müller-Eschner M, Amarteifio E, Bäuerle T, Weber MA, Kauczor HU, Rengier F. Dynamic contrast-enhanced magnetic resonance imaging: fundamentals and application to the evaluation of the peripheral perfusion. Cardiovasc Diagn Ther. 2014;4:147–164.
6. DCE MRI Technical Committee. DCE MRI Quantification Profile, Quantitative Imaging Biomarkers Alliance. Version 1.0. Reviewed Draft. QIBA, July 1, 2012. Available from: http://rsna.org/QIBA_.aspx
7. Shukla-Dave A, Obuchowski NA, Chenevert TL, Jambawalikar S, Schwartz LH, Malyarenko D, Huang W, Noworolski SM, Young RJ, Shiroishi MS, Kim H, Coolens C, Laue H, Chung C, Rosen M, Boss M, Jackson EF. Quantitative imaging biomarkers alliance (QIBA) recommendations for improved precision of DWI and DCE-MRI derived biomarkers in multicenter oncology trials. J Magn Reson Imaging 2019;49:e101–e121.
8. Furman-Haran E, Feinberg MS, Badikhi D, Eyal E, Zehavi T, Degani H. Standardization of radiological evaluation of dynamic contrast enhanced MRI: application in breast cancer diagnosis. Technol Cancer Res Treat. 2014;13:445–454.
9. Sourbron SP, Buckley DL. Tracer kinetic modelling in MRI: estimating perfusion and capillary permeability. Phys Med Biol. 2012;57:R1–R33.
10. Caravan P, Farrar CT, Frullano L, Uppal R. Influence of molecular parameters and increasing magnetic field strength on relaxivity of gadolinium- and manganese-based T1 contrast agents. Contrast Media Mol Imaging. 2009;4:89–100.
11. Rohrer M, Bauer H, Mintorovitch J, Requardt M, Weinmann HJ. Comparison of magnetic properties of MRI contrast media solutions at different magnetic field strengths. Invest Radiol. 2005;40:715–724.
12. Moser E, Laistler E, Schmitt F, Kontaxis G. Ultra-high field NMR and MRI–the role of magnet technology to increase sensitivity and specificity. Front Phys. 2017;5:33.
13. Jacobs I, Hectors SJ, Schabel MC, Grull H, Strijkers GJ, Nicolay K. Cluster analysis of DCE-MRI data identifies regional tracer-kinetic changes after tumor treatment with high intensity focused ultrasound. NMR Biomed. 2015;28:1443–1454.
14. Aryal MP, Nagaraja TN, Brown SL, Lu M, Bagher-Ebadian H, Ding G, Panda S, Keenan K, Cabral G, Mikkelsen T, Ewing JR. Intratumor distribution and

test-retest comparisons of physiological parameters quantified by dynamic contrast-enhanced MRI in rat U251 glioma. NMR Biomed. 2014;27:1230–1238.
15. Vonken EP, van Osch MJ, Bakker CJ, Viergever MA. Simultaneous quantitative cerebral perfusion and Gd-DTPA extravasation measurement with dual-echo dynamic susceptibility contrast MRI. Magn Reson Med. 2000;43:820–827.
16. Quarles CC, Gore JC, Xu L, Yankeelov TE. Comparison of dual-echo DSC-MRI- and DCE-MRI-derived contrast agent kinetic parameters. Magn Reson Imaging. 2012;30:944–953.
17. de Bazelaire C1, Rofsky NM, Duhamel G, Zhang J, Michaelson MD, George D, Alsop DC. Combined T2* and T1 measurements for improved perfusion and permeability studies in high field using dynamic contrast enhancement. Eur Radiol. 2006;16:2083–2091.
18. Kleppesto M, Larsson C, Groote I, Salo R, Vardal J, Courivaud F, Bjørnerud A. T2*-correction in dynamic contrast-enhanced MRI from double-echo acquisitions. J Magn Reson Imaging. 2014;39:1314–1319.
19. Zhang J, Freed M, Winters K, Kim SG. Effect of T2* correction on contrast kinetic model analysis using a reference tissue arterial input function at 7 T. MAGMA. 2015;28:555–563.
20. Ewing JR, Bagher-Ebadian H. Model selection in measures of vascular parameters using dynamic contrast-enhanced MRI: experimental and clinical applications. NMR Biomed. 2013;26:1028–1041.
21. Heilmann M, Walczak C, Vautier J, Dimicoli JL, Thomas CD, Lupu M, Mispelter J, Volk A. Simultaneous dynamic T1 and T2* measurement for AIF assessment combined with DCE MRI in a mouse tumor model. MAGMA. 2007;20:193–203.
22. Cebulla J, Huuse EM, Pettersen K, van der Veen A, Kim E, Andersen S, Prestvik WS, Bofin AM, Pathak AP, Bjørkøy G, Bathen TF, Moestue SA. MRI reveals the in vivo cellular and vascular response to BEZ235 in ovarian cancer xenografts with different PI3-kinase pathway activity. Br J Cancer. 2015;112:504–513.
23. Kim E, Tunset HM, Cebulla J, Vettukattil R, Helgesen H, Feuerherm AJ, Engebråten O, Mælandsmo GM, Johansen B, Moestue SA. Anti-vascular effects of the cytosolic phospholipase A2 inhibitor AVX235 in a patient-derived basal-like breast cancer model. BMC Cancer. 2016;16:191.
24. Gingrich JR, Greenberg NM. A transgenic mouse prostate cancer model. Toxicol Pathol. 1996;24:502–504.
25. Hill DK, Kim E, Teruel JR, Jamin Y, Widerøe M, Søgaard CD, Størkersen Ø, Rodrigues DN, Heindl A, Yuan Y, Bathen TF, Moestue SA. Diffusion-weighted MRI for early detection and characterization of prostate cancer in the transgenic adenocarcinoma of the mouse prostate model. J Magn Reson Imaging. 2016;43:1207–1217.
26. Kim J, Kim E, Euceda LR, Meyer DE, Langseth K, Bathen TF, Moestue SA, Huuse EM. Multiparametric characterization of response to anti-angiogenic therapy using USPIO contrast-enhanced MRI in combination with dynamic contrast-enhanced MRI. J Magn Reson Imaging. 2018;47:1589–1600.
27. Noebauer-Huhmann IM, Szomolanyi P, Juras V, Kraff O, Ladd ME, Trattnig S. Gadolinium-based magnetic resonance contrast agents at 7 Tesla: in vitro T1 relaxivities in human blood plasma. Invest Radiol. 2010;45:554–558.
28. Jensen LR, Berge K, Bathen TF, Wergedahl H, Schønberg SA, Bofin A, Berge RK, Gribbestad IS. Effect of dietary tetradecylthioacetic acid on colon cancer growth studied by dynamic contrast enhanced MRI. Cancer Biol Ther. 2007;6:1810–1816.
29. Tofts PS, Brix G, Buckley DL, Evelhoch JL, Henderson E, Knopp MV, Larsson HB, Lee TY, Mayr NA, Parker GJ, Port RE, Taylor J, Weisskoff RM. Estimating kinetic parameters from dynamic contrast-enhanced T(1)-weighted MRI of a diffusable tracer: standardized quantities and symbols. J Magn Reson Imaging. 1999;10:223–232.
30. Blockley NP, Jiang L, Gardener AG, Ludman CN, Francis ST, Gowland PA. Field strength dependence of R1 and R2* relaxivities of human whole blood to ProHance, Vasovist, and deoxyhemoglobin. Magn Reson Med. 2008;60:1313–1320.
31. Sourbron S, Heilmann M, Biffar A, Walczak C, Vautier J, Volk A, Peller M. Bolus-tracking MRI with a simultaneous T1- and T2*-measurement. Magn Reson Med. 2009;62:672–681.
32. Semmineh NB, Xu J, Skinner JT, Xie J, Li H, Ayers G, Quarles CC. Assessing tumor cytoarchitecture using multiecho DSC-MRI derived measures of the transverse relaxivity at tracer equilibrium (TRATE). Magn Reson Med. 2015;74:772–784.
33. Bedard PL, Hansen AR, Ratain MJ, Siu LL. Tumour heterogeneity in the clinic. Nature. 2013;501:355–364.
34. O'Connor JP, Jackson A, Parker GJ, Roberts C, Jayson GC. Dynamic contrast-enhanced MRI in clinical trials of antivascular therapies. Nat Rev Clin Oncol. 2012;9:167–177.
35. Padhani AR, Khan AA. Diffusion-weighted (DW) and dynamic contrast-enhanced (DCE) magnetic resonance imaging (MRI) for monitoring anticancer therapy. Target Oncol. 2010;5:39–52.
36. Roberts C, Issa B, Stone A, Jackson A, Waterton JC, Parker GJ. Comparative study into the robustness of compartmental modeling and model-free analysis in DCE-MRI studies. J Magn Reson Imaging. 2006;23:554–563.
37. Loveless ME, Halliday J, Liess C, Xu L, Dortch RD, Whisenant J, Waterton JC, Gore JC, Yankeelov TE. A quantitative comparison of the influence of individual versus population-derived vascular input functions on dynamic contrast enhanced-MRI in small animals. Magn Reson Med. 2012;67:226–236.